Virus#Templated Nickel Phosphide Nanofoams as Additive#Free, Thin#Film Li#Ion Microbattery Anodes

Citation: Records, William C. et al. "Virus#Templated Nickel Phosphide Nanofoams as Additive# Free, Thin#Film Li#Ion Microbattery Anodes." Small 15, 44 (September 2019): 1903166 © 2019 Wiley

As Published: http://dx.doi.org/10.1002/smll.201903166

Publisher: Wiley

Persistent URL: https://hdl.handle.net/1721.1/123308

Version: Author's final manuscript: final author's manuscript post peer review, without publisher's formatting or copy editing

Virus-templated nickel phosphide nanofoams as additive-free, thin-film Li-ion microbattery anodes

*William C. Records, Shuya Wei, Angela M. Belcher**

W. C. Records, Dr. S. Wei, Prof. A. M. Belcher
Koch Institute for Integrative Cancer Research
Massachusetts Institute of Technology
500 Main Street, Cambridge, MA 02139, USA
E-mail: belcher@mit.edu

W. C. Records
Department of Chemical Engineering
Massachusetts Institute of Technology
77 Massachusetts Avenue, Cambridge, MA 02139, USA

Dr. S. Wei, Prof. A. M. Belcher
Department of Materials Science and Engineering
Massachusetts Institute of Technology
77 Massachusetts Avenue, Cambridge, MA 02139, USA

Prof. A. M. Belcher
Department of Biological Engineering
Massachusetts Institute of Technology
77 Massachusetts Avenue, Cambridge MA 02139, USA

Keywords: 3D nanostructure, transition metal phosphide, biotemplating, M13 bacteriophage, Li-ion microbattery

Transition metal phosphides are a new class of materials generating interest as alternative negative electrodes in lithium-ion batteries. However, metal phosphide syntheses remain underdeveloped in terms of simultaneous control over phase composition and 3D nanostructure. Herein, M13 bacteriophage is employed as a biological scaffold to develop 3D nickel phosphide nanofoams with control over a range of phase compositions and structural elements. Virus-templated Ni_5P_4 nanofoams are then integrated as thin-film negative electrodes in lithium-ion microbatteries, demonstrating a discharge capacity of 677 mAh g^{-1} (677 mAh cm^{-3}) and an 80% capacity retention over more than 100 cycles. This strong electrochemical performance is attributed to the virus-templated, nanostructured morphology, which remains electronically conductive throughout cycling, thereby sidestepping the need for

conductive additives. When accounting for the mass of additional binder materials, virus-templated Ni_5P_4 nanofoams demonstrate the highest practical capacity reported thus far for Ni_5P_4 electrodes. Looking forward, this synthesis method is generalizable and could enable precise control over 3D nanostructure and phase composition in other metal phosphides, such as cobalt and copper.

1. Introduction

Lithium-ion microbatteries are integral in devices spanning microelectronics, medical implants, and telecommunications.[1] Due to constraints on electrode size and thickness, microbattery performance is necessarily dependent on the design of active, 3D nanostructured electrodes.[2] At the negative electrode, typically comprising Si,[3–5] SnO_2,[6,7] or Ge,[8] a high theoretical capacity comes at the price of large volumetric expansion due to the insertion of Li^+.[9] One potential solution lies in the use of conversion anodes, which react with, rather than intercalate, Li^+ during discharge. Over the last several decades, several classes of materials have emerged as possible conversion anodes for both micro- and macrobatteries, such as transition metal oxides,[10] carbides,[11] and sulfides.[12] In particular, metal phosphides have displayed strong performance in both lithium-ion[13–15] and sodium-ion[16–19] batteries, owing to their high capacity, good electronic conductivity, and naturally abundant constituent elements.

Despite their technological promise, synthesis of metal phosphides has traditionally been challenging due to the flammability and toxicity of common phosphorus-containing precursors.[20] Simultaneous control over nanostructure, crystal structure, and surface morphology remains imprecise, thereby impeding electrode design and incorporation into devices. Moreover, most reported metal phosphide synthesis routes produce lower dimensional nanomaterials, such as 1D nanoparticles and nanorods and 2D nanosheets.[21,22] Using strongly coordinated, organic phosphorus precursors like trioctylphosphine, these

interesting, lower dimensional nanostructures can form spontaneously. However, they must be further mixed with conductive carbons and binders in a post-synthesis step and are difficult to integrate into microbattery-scale electrodes. Meanwhile, the relative electrochemical inertness of additives substantially reduces the practical energy density of the electrodes. Few synthesis routes are available for 3D nanostructures with a predefined morphology and additive-free integration into electrodes. Thus, there is a need for a metal phosphide synthesis that can address this gap.

One less-explored approach taken to design 3D nanostructures is to employ biological organisms as scaffolds. Filamentous-type bacteriophage viruses, such as M13, have generated great research interest as a tool in synthesizing nanostructured materials. M13 virus particles are highly anisotropic, approximately 880 nm long and 6.5 nm in diameter. Additionally, the viral DNA offers a genetic handle to modulate the binding capacity of the exterior coat proteins for a variety of organic and inorganic materials.[23] Due to its unique shape and binding precision, M13 enables simultaneous control of both nanoscale morphology and material properties. This capability is unique among other similar 3D electrode support materials, such as carbon nanotubes and metal foams, and enables tunability across all aspects of electrode design. The virus has been successfully incorporated into energy storage systems in the past, including lithium-air,[24] lithium-ion, [25,26] and sodium-ion[27,28] batteries. More recently, facile crosslinking methods applied to M13 virus particles have yielded a porous, tunable nanofoam scaffold, compatible with the design of an additive-free, thin-film electrode.[29] Virus-templated nanofoams are an ideal 3D architecture for microbattery electrodes due to their excellent Li^+ ion and electronic transport properties, accommodation of volumetric changes during cycling, and tunable morphological features.

Herein, we report the synthesis of 3D nanostructured, nickel phosphide nanofoams, made possible by leveraging the unique advantages of material design with M13 bacteriophage including its nanoscopic proportions and tunability of binding affinity. Virus particles were

crosslinked into thin, porous gels, which acted as nanofoam scaffolds for the synthesis of different nickel phosphides. The gel scaffolds proved to form mechanically robust architectures and did not require additional binders or conductive additives upon integration into a microbattery electrode. Films were then tested as additive-free, negative electrodes in lithium-ion microbatteries, demonstrating excellent electrochemical performance among additive-free formulations: up to 677 mAh g^{-1} and 677 mAh cm^{-3} capacity with 80% capacity retention over 100 cycles. This strong performance is attributed to the virus-templated, nanostructured morphology of the nanofoams, which remains electrically conductive throughout charge and discharge. Our materials demonstrate the highest practical capacity of any Ni_5P_4 electrode when accounting for the additional mass of conductive agents and binders in other electrode materials. Looking forward, the metal phosphide synthesis strategy presented here can be further generalized to other transition metals, such as Cu or Co. Furthermore, the virus-templated scaffold approach is compatible with implementation in other battery chemistries and device architectures.

2. Results and Discussion

2.1. Virus-Templated TMP Synthesis

Virus-templated nickel phosphide nanofoams were synthesized in a generalizable, three-step procedure, summarized in **Figure 1**. First, M13 virus particles displaying the negatively charged peptide sequence E–E–A–E were chemically crosslinked with glutaraldehyde to form a virus hydrogel on a titanium current collector. The crosslinking reaction is facile and independent of which virus clone is used. Unlike similar support materials, such as carbon nanotubes, virus particles do not require further surface functionalization before subsequent synthesis steps. We chose the EEAE clone, as it has been shown to bind well to divalent metal cations in a number of different applications.[28,30] Taking advantage of this binding affinity, the virus hydrogels were metallized using an electroless deposition (ELD) bath with sodium

hypophosphite acting as the reducing agent. Unlike other common reducing agents, such as dimethylamine borane, hydrazine, or sodium borohydride, sodium hypophosphite can spontaneously co-deposit phosphorus as a side reaction to the intended metal reduction.[31] Accordingly, an alloy of nickel and phosphorus (Ni–P) with up to 12 wt% phosphorus was deposited onto the crosslinked scaffold. Virus-templated nanofoams are characterized by an interconnected and contiguous network of nanowires with controllable diameters between 60 and 200 nm.[29] As-deposited Ni–P nanofoams were then subjected to a low-temperature heat treatment to produce the corresponding nickel phosphide. Because phosphorus is co-deposited with nickel during ELD, the Ni_3P phase forms spontaneously upon heating Ni–P nanofoams. However, the maximum phosphorus content attainable via ELD plateaus near 25 at% P, limiting the potential crystal phases to Ni and Ni_3P in this material.[31,32]

In order to synthesize increasingly phosphorus-rich nickel phosphides, an additional phosphorus source was required. Sodium hypophosphite is the most prevalent source used for this purpose and has been applied extensively in transition metal phosphide syntheses.[21,33,34] In a similar fashion to previous reports, NaH_2PO_2 was thermally degraded *in situ* to produce small amounts of phosphine, which reacted with the virus-templated Ni–P nanofoams to form various nickel phosphide phases with up to 44 at% P (Ni_5P_4). Other intermediate phosphide phases, including Ni_2P, were also accessible using this methodology. Upon optimizing the parameters of the heat treatment, we produced nanofoams with a controllable phase composition: Ni_3P, Ni_2P, and Ni_5P_4.

Scanning electron microscopy (SEM) images of Ni–P, Ni_3P, Ni_2P, and Ni_5P_4 nanofoams are shown in **Figure 2**. While the nanowire struts are clearly changed by heat treatment, namely for crystal phases with a higher phosphorus content, the overall porous, interconnected morphology of the nanofoam remains unchanged. Analogous transformations in the nanowire morphology are observed in transmission electron microscopy (TEM) images in **Figure 3**, with the virus-containing cores of the nanowires clearly visible. As the

phosphorus content of the nanowires increases, the surface of the wires becomes rougher, and nickel phosphide crystallites begin protruding from the surface.

The crystallography of the virus-templated nickel phosphide nanofoams was confirmed using high-resolution TEM (HRTEM) and X-ray diffraction (XRD) in **Figures 3** and **4a**, respectively. In **Figure 3**, Ni–P nanofoams displayed a largely amorphous structure with a broad peak centered around the (111) plane of FCC nickel. This result is typical for electroless nickel deposits with high phosphorus content (>10 wt%).[31] Upon heat treatment, the as-deposited material crystallized into one of several nickel phosphide phases, Ni_3P, Ni_2P, or Ni_5P_4, which were all confirmed by XRD and multiple lattice fringes in HRTEM. Thus, the virus-templated synthesis method clearly enables control over both nanoscale morphological features and phosphide phase.

X-ray photoelectron spectroscopy (XPS) yielded similar spectra among each of the metal phosphides, shown in **Figure 4b**. The Ni $2p^{3/2}$ peak was fitted to 852.1 eV, 852.5 eV, 852.8 eV, and 853.0 eV for Ni–P, Ni_3P, Ni_2P, and Ni_5P_4, respectively. Similarly, the P $2p^{3/2}$ peak was fitted to 129.0 eV, 129.4 eV, 129.3 eV, and 129.2 eV. The shifts toward larger Ni binding energies and smaller P binding energies with increased phosphidation among the crystallized metal phosphides also indicate that Ni atoms gain a slightly more positive charge and P atoms gain a slightly more negative charge with increased phosphidation. The two trends suggest that there is a transfer of electrons from nickel to phosphorus in each of the nickel phosphide phases. This is unsurprising given that phosphorus is somewhat more electronegative than nickel and has also been reported elsewhere.[35]

The morphology of the virus-templated nickel phosphide thin films was explored in the z-dimension as well (**Section S.1**). Thickness profiles for each nickel phosphide phase can be found in **Figure S1**. Virus-templated Ni–P thin films were 18.4 ± 3.0 μm thick. After heat treatment to form Ni_3P, Ni_2P, or Ni_5P_4 phases, the thickness shrank drastically to 9.1 ± 1.3 μm, 6.2 ± 1.9 μm, and 6.6 ± 0.6 μm, respectively (**Table 1**). The nickel phosphide thin films

would be particularly well-suited for microbattery applications, in which the total cell thickness is typically less than 15 μm.[36] The elemental distribution of elements was probed using SEM–energy dispersive X-ray spectroscopy (SEM–EDX) to explore determine if phosphidation yielded a homogeneous material in the z-dimension. As reported in **Figure S2**, the nickel and phosphorus distribution throughout the tested Ni_5P_4 nanofoam was indeed homogeneous. For monophasic Ni_5P_4, the corresponding measurement of the Ni:P ratio was 56.1:43.9, matching the theoretical 5:4 ratio well. To corroborate this elemental analysis, inductively coupled plasma–atomic emission spectroscopy (ICP–AES) was performed on three replicates of each virus-templated nickel phosphide nanofoam phase. The elemental composition is reported in **Table 1** and matches well with the predicted atomic ratios of Ni and P.

Nickel and phosphorus can form mixtures of intermetallics with a range of stoichiometries depending on the overall composition, making the formation of monophasic materials difficult.[32] At the same time, the volume changes associated with thermal stress and phase change during phosphidation can degrade a nanoscale 3D support structure, limiting control over supported metal phosphide nanostructures. Many reported syntheses of metal phosphide nanoparticles offer well-defined control over morphology and phase composition (reviewed extensively in Ref. [20]). Nanoparticles are less attractive as electrode materials in microbatteries than 3D nanostructures, however, as they typically require conductive additives to avoid the capacity fading and conductivity problems associated with cycling-induced aggregation.[37]

Several of these metal phosphide syntheses employ a gas-solid reaction, similar to the heat treatment step reported in this work, to produce a metal phosphide supported on a 3D metal structure.[18,38] Control of phase composition remains limited in these cases, as the metal support is not fully converted into a metal phosphide. Even without the use of conductive additives, these electrodes have a lower practical capacity likely stemming from the mass

contribution of the less active, unreacted, metal support. Moreover, most 3D supports, such as nickel foams, are difficult to integrate into a microbattery due to their macroscopically large struts and pores. In some cases, phosphidation yields an interesting, textured, nanoscale morphology on the support surface.[38] Such surface features are coincidental, however, and difficult to control synthetically.

Conversely, the virus-templated synthesis described here offers orthogonal control over metal phosphide phase and a contiguous 3D nanoscale morphology. The result is a nanostructured, thin-film metal phosphide, grown directly on a current collector without the use of conductive additives and characterized by feature sizes compatible with microbattery electrode dimensions (typically less than 15 μm thick).[1] We found heat treatment to be the most critical step in producing a monophasic material with a well-defined, 3D contiguous nanostructure with smaller struts and pores. The synthesis must align the different timescales for several processes, including the thermal degradation of sodium hypophosphite, transport of the phosphine generated *in situ* to the nanofoam, reaction with the nanofoam, and crystallization of the metal phosphide. Coordinating these timescales is essential to achieving reproducible results. Poorly optimized phosphidation conditions can lead to phase impurities or destruction of the 3D morphology via pore occlusion, sintering, or thermal cracking. Examples of the problems arising from a poorly optimized heat treatment are reported in **Figure S3,** and suggestions for optimizing phosphidation conditions can be found in **Section S.2** in the Supporting Information.

2.2. Electrochemical Characterization

The electrochemical activity of the virus-templated nickel phosphide nanofoams as negative electrodes in lithium-ion batteries was tested, and the results are reported in **Figure 5**. As a benefit from their unique synthesis, virus-templated nickel phosphide nanofoams can be directly utilized as freestanding anodes without the addition of any

conductive carbon or polymeric binders. Galvanostatic cycling experiments with different nickel phosphide phases are shown in **Figure 5a**. Virus-templated Ni_5P_4 nanofoams greatly outperformed corresponding Ni_3P and Ni_2P nanofoams, displayed the highest specific capacity, and consequently were investigated more thoroughly for the remainder of this work. The trend between the level of phosphidation and specific capacity can be attributed to the electrochemical reaction mechanism between Li^+ ions and nickel phosphide, which involves intercalation and conversion. During discharge, it has been proposed that lithium ions first intercalate with Ni_xP_y to form $LiNi_xP_y$ complexes, followed by conversion to Li_3P and Ni metal.[39] Nickel phosphides with higher phosphorus content will yield stoichiometrically more Li_3P during discharge and therefore have intrinsically higher theoretical capacities. It is expected that extending the virus-templated structure to more P-rich nickel phosphides, such as NiP and NiP_2, would continue this trend.

Upon cycling, the specific and volumetric capacities of virus-templated Ni_5P_4 nanofoams, initially 677 mAh g^{-1} and 677 mAh cm^{-3}, decreased 20% before stabilizing to a characteristic voltage profile with reversible capacities of 540 mAh g^{-1} and 540 mAh cm^{-3} (**Figure 5b**). This stems from material and crystal rearrangement during the initial cycles. The rate capability of the virus-templated Ni_5P_4 nanofoam anode is shown in **Figure 5c** and **Figure S4**. At fast cycling rates of 100, 200, 300, and 400 mA g^{-1}, stable specific capacities of 473, 396, 257, and 113 mAh g^{-1}, respectively, were achieved. Virus-templated Ni_5P_4 nanofoams demonstrated a high, reversible capacity between 500 and 600 mAh g^{-1} at a cycling rate of 50 mA g^{-1}, which remained stable for over 100 cycles (**Figure 5d**). The performance described here is among the best reported for nickel phosphide electrodes in literature (**Table S1**). Furthermore, virus-templated Ni_5P_4 nanofoams demonstrate the highest practical capacity of any Ni_5P_4 material reported thus far, calculated considering the total mass of the electrode material. This measure includes the mass of the non-conductive M13 scaffold for virus-templated electrodes, which accounts for less than 1% of the total mass (**Section S.3**).

Considering that virus-templated Ni_5P_4 electrodes lack conductive additives, their unique nanostructure likely plays an important role in facilitating their electrochemical performance. Using a virus-templated, 3D nanofoam enables the formation of a conductive nickel network during discharge, which facilitates electronic transport without additional inactive components. In terms of volumetric capacity, further improvements are expected for denser nanofoams.[40,41] Traditional solid-processing strategies for increasing overall density, such as tapping, are not applicable for our solution-processed materials. Several experimental parameters, however, such as the virus particle concentration and ELD time, have previously been shown to increase crosslinking density and decrease porosity.[29]

The lithiation and delithiation mechanism for virus-templated Ni_5P_4 negative electrodes was explored using cyclic voltammetry (CV), shown in **Figure 5e**. Voltammograms reveal two anodic peaks at 1.0 and 1.2 V vs. Li/Li^+ during charge and two cathodic peaks at 0.35 and 0.6 V vs. Li/Li^+ during discharge. The appearance of two peaks is indicative of an insertion-conversion mechanism, as discussed above.[15,18] Under this mechanism, lithium ions first insert into the Ni_5P_4 lattice to form $Li_xNi_5P_4$ before undergoing conversion to Li_3P and Ni metal. The magnitude of the insertion peak is larger than that for extraction, which indicates that the rate of insertion is faster than the rate of extraction.[42] The currents at the voltammogram peaks were used to estimate Li^+ diffusivity on the order of 10^{-11} cm^2 s^{-1} for the electrochemical reaction steps related to insertion and conversion (**Figure 5e inset, Section S.4**). The lithiation mechanism was further corroborated by the formation of nanocrystalline domains for Li_3P, observable with HRTEM (**Figure S5**).

Volume expansion upon lithiation was observed, as evidenced by cracks appearing after even the first discharge (**Figure S5**). The nanowires, however, maintained their structure throughout cycling, up to 100 cycles (**Figure 6a-c**). This corroborates the formation of conductive Ni wires during discharge, one of the advantages imparted by the virus-templated nanostructure. However, after a single lithiation step, the long-range crystallinity of the

nanowire is broken, leaving only amorphous and nanocrystalline domains. We performed further CV tests to compare samples undergoing their 1st and 10th cycles (**Figure S6**). The two peaks related to insertion and conversion persist through the 10th cycle, indicating good electrode reversibility and a consistent mechanism throughout the lifetime of the cell. After 100 cycles, the nanowires appear completely amorphized and roughened by repeated lithiation and delithiation, and an SEI layer is present (**Figure 6d**). Nevertheless, even after extensive cycling, the contiguous and interconnected nature of the porous nanofoam morphology is preserved (**Figure S7**). Overall, the virus-templated electrodes maintain both ionic and electronic conductivity during cycling, which likely leads to the improved resistance against capacity fading that is observed.

Discharged virus-templated Ni_5P_4 nanofoams were examined via *ex situ* XPS after 100 cycles (**Figure 6e**). The expected discharge products, including Ni, Li_xP, and Li_3P, were positively identified. Several other lithium compounds were also observed, including $LiCO_3$, $LiPO_4$, and LiF, likely from the degradation of the electrolyte during cycling. Appreciable XPS signal from the electrodes required extensive milling from an argon ion beam, suggesting the formation a solid-electrolyte interphase (SEI) layer at the electrode surface.

Electrochemical impedance spectroscopy (EIS) was performed, and an equivalent circuit was modeled on pristine and cycled samples (**Figure 6f**). Nyquist plots comprised two overlapping semicircles in the high and medium frequency regions and a linear feature in the low frequency region. Attributing impedance features to physical phenomena is not always straightforward or clear. Following one commonly used interpretation, we assigned the semicircles to interphase contact resistance (R_i) and charge transfer resistance (R_{ct}) and the linear region to Li^+ diffusion-related impedance.[43–45] The diameter of the high-frequency semicircle increases with cycling. From this trend, we hypothesize that R_i, which should account for electron transport from the current collector to the reaction sites, originates from an increasingly thick SEI layer. This provides additional evidence to the XPS and TEM data

shown in **Figures 6d–e**. Growth of the SEI layer also likely contributes to the initial capacity fading observed in the first 20 cycles before plateauing at a reversible capacity of 540 mAh g^{-1} (**Figure 5d**). On the other hand, the diameter of the second semicircle decreases with cycling. From this trend, R_{ct}, which accounts for resistance occurring at the reaction sites, may decrease with greater amorphization of the active material. This suggests that the reaction to form Li_3P may be more facile in an amorphous active material. Further details on the equivalent circuit modeling are given in **Section S.6**

3. Conclusion

In summary, we developed a virus-templated methodology to produce 3D nickel phosphide nanofoams with a consistent nanoscale morphology and with tunable phase composition (Ni–P, Ni_3P, Ni_2P, and Ni_5P_4). Unlike previous reports, virus-templating offers simultaneous control of phosphide phase and 3D nanostructure, thereby enabling greater versatility for optimization in devices. The nanostructure was then integrated as an additive-free, thin-film, lithium-ion microbattery electrode. Virus-templated Ni_5P_4 nanofoams display strong and stable performance, including 80% capacity retention of the initial 677 mAh g^{-1} (677 mAh cm^{-3}) discharge capacity over 100 cycles. Analysis of the electrochemical performance of the nickel phosphide nanofoams during cycling further corroborated the both the reaction mechanism and preservation of the 3D nanostructured morphology.

Virus-templated nickel phosphide nanofoams offer two main advantages over other materials and morphologies as microbattery electrodes. First, the contiguous and interconnected nanostructure ensures good electronic and ionic conductivity throughout cycling. This intrinsic conductivity nullifies the typical requirement of conductive additives and binders and leads to the highest practical capacity of any reported Ni_5P_4 electrode. Second, these findings suggest that the 3D virus-templated nanoarchitecture is translatable to

other metal phosphides and therefore this method reported here offers a general synthesis strategy for creating 3D nanostructured, thin-film electrodes for microbattery applications.

4. Experimental Section

M13 bacteriophage growth and culturing: Concentrated stocks of metal-cation-binding EEAE M13 phage were prepared via the infection of XL1-Blue *Escherichia coli* bacteria (Agilent Technologies) with M13, amplification in a GE WAVE Bioreactor 20/50 system, and purification via hollow-fiber filtration and PEG-NaCl precipitation using previously reported methods.[29,30]

Synthesis of virus-templated nanofoams: Nanofoams were prepared by adapting previously reported methods.[29,30] Briefly, 10 μL of 2.0×10^{13} plaque-forming units (pfu) mL^{-1} M13 was pipetted onto Ti foil (0.127 mm thick, 99.99%, Fisher Scientific, previously punched into 1 cm diameter discs and washed with ethanol and acetone). The Ti foil substrate was then placed droplet-side down onto a static glutaraldehyde solution (50/50 (w/w), Sigma-Aldrich). After 60 minutes, the now cross-linked M13 virus hydrogel was removed and dialyzed in ultrapure water (Millipore Type 1, 18.2 MΩ cm) for 12–18 hours. Next, 25 μL of 10 mM Na_2PdCl_4 (98%, Sigma-Aldrich) was pipetted onto the hydrogel and incubated for six hours without drying before rinsing for 30 to 60 seconds in ultrapure water. Virus-templated Ni–P nanofoams were synthesized by metallizing the nickel-phosphorus alloy directly onto the phage network with a previously reported sodium hypophosphite-based ELD bath[29] for 60 minutes, followed by 15 minutes of rinsing in ultrapure water and drying under vacuum overnight. To control for differences in post-deposition properties (such as degree of crystallinity) due to variable phosphorus content, all samples were subjected to identical ELD times, yielding the Ni–P compositions reported in **Table 1**.

Phosphidation of nanofoams: $NaH_2PO_2 \cdot H_2O$ (≥99%, Sigma-Aldrich) was weighed out in a high-precision balance to achieve a particular P:Ni molar ratio. For typical virus-templated Ni_2P and Ni_5P_4 nanofoams, the molar ratio of P:Ni was 3:1 and 75:1, respectively. The hypophosphite salt was pushed into a tight pile in a 5 cm long, open crucible approximately 1 cm upstream of the Ti substrate with the Ni–P nanofoam. The crucible contents were then heated to 300 °C for 2 hours with a 20°C min^{-1} ramp rate under flowing argon atmosphere (>200 SLPM, set by Alicat Scientific MC mass flow controller). Virus-templated Ni_3P nanofoams were synthesized using identical heat-treatment procedures, but without any NaH_2PO_2 present. Nanofoams were stored under vacuum or argon atmosphere to minimize post-synthesis oxidation before cell assembly.

Cell assembly and testing: 2032 coin-type cells were assembled using 99.9% Li metal foil (0.75 mm thick, Alfa-Aesar) as the anode, glass fiber membranes as the separator (Whatman Grade 934-AH, Sigma-Aldrich), virus-templated nanofoams on Ti foil as the cathode, and 80 μL of electrolyte (1.0 M $LiPF_6$ in EC/DEC = 50/50 (v/v), battery grade, Sigma-Aldrich). Cell assembly was carried out in an argon-filled glovebox (MBraun Labmaster). The typical areal mass loading for virus-templated Ni_3P, Ni_2P, and Ni_5P_4 electrodes were 0.25, 0.34, and 0.66 mg cm^{-2}, respectively. The room-temperature cycling characteristics of the cells were evaluated under galvanostatic conditions using Land battery testers, and electrochemical processes in the cells were studied by cyclic voltammetry and impedance spectroscopy using a Biologic VMP-3 potentiostat. Electrochemical impedance was measured between 200 kHz and 0.1 Hz with a perturbation amplitude of 10mV on a pristine cell, as well as cells cycled at 50 mA g^{-1} in 1–3 V for 10 or 100 cycles. The equivalent circuit model was fitted using EC-Lab software. Volumetric capacity was approximated using the total geometric areas of the electrodes and their average thicknesses reported in **Table 1**.

Post-electrochemical treatment: Virus-templated nickel phosphide electrodes were harvested after electrochemical measurements by disassembling the coin cells. The electrodes

were washed with the electrolyte solvent EC/DEC = 50/50 (v/v) at least three times to remove the excess electrolyte salt and dried under a vacuum chamber. All procedures were carried out in an argon-filled glovebox to avoid air oxidation.

Physical characterization: SEM–EDX was performed using a Helios Nanolab 600 dual beam focused ion beam milling system and a JEOL 6700 microscope. TEM and HRTEM images were acquired with a JEOL 2100 FEG microscope operating at 200 kV. XRD was performed using a PANalytical X'Pert Pro multipurpose diffractometer XRPD with a 1.8 kW sealed X-ray source, a Cu target (kα = 0.15418 nm), and a generator set at 45 kV and 40 mA. 2θ scans were measured from 20° to 90° with an angular step size of 0.017° and a scanning rate of 0.038°/sec. Samples were prepared on silicon wafers (Type P, <100>, Ted Pella, Inc.), and a 5° ω-shift was applied during measurement to correct for the presence of the silicon peaks. XPS was performed using a Physical Electronics Versaprobe II spectrometer with an Al K_α (1486.6 eV) photon source and a 23.5 eV pass energy. Peak deconvolution was performed using CasaXPS software with a Shirley background. Pristine nickel phosphide nanofoam spectra were charge-corrected using the 284.8 eV peak in the adventitious carbon 1s region (C 1s). Peaks in the C 1s region resulted in unreliable charge correction values for *ex situ* samples, however, as most carbon species were removed by the ion milling required to penetrate the SEI layer on the electrode surface. Further, differential charging between the SEI layer and the active electrode material resulted in peak positions at lower binding energies than expected. Thus, for all samples examined *ex situ*, zero-valent Ni, representing another discharge product, was used for charge correction.[46] ICP-AES was conducted using an Agilent 5100 DVD spectrometer. Film thickness was measured using a Veeco Dektak 150 surface profiler.

Further details of the crystal structure investigation(s) may be obtained from the Fachinformationszentrum Karlsruhe, 76344 Eggenstein-Leopoldshafen (Germany), on quoting the depository numbers CSD-1913659 through CSD-1913661

Supporting Information
Supporting Information is available from the Wiley Online Library or from the author.

Acknowledgements

Funding for this work was provided by the U.S. Defense Advanced Research Projects Agency Living Foundries program award number HR0011835402 and by Shell International Exploration & Production, Inc.'s Electrochemical Catalysis & Light-Driven Chemical Production award number 4550155123. This work made use of the MRSEC Shared Experimental Facilities supported by the National Science Foundation under award number DMR-1419807. We thank Dr. Dong Soo Yun at the Koch Institute Swanson Biotechnology Center for his assistance with HRTEM, HAADF–STEM, and EDX.

References

[1] L. Fan, S. Wei, S. Li, Q. Li, Y. Lu, *Adv. Energy Mater.* **2018**, *8*, 1702657.

[2] J. H. Pikul, H. Gang Zhang, J. Cho, P. V. Braun, W. P. King, *Nat. Commun.* **2013**, *4*, 1732.

[3] C. K. Chan, H. Peng, G. Liu, K. McIlwrath, X. F. Zhang, R. A. Huggins, Y. Cui, *Nat. Nanotechnol.* **2008**, *3*, 31.

[4] H. Wu, G. Chan, J. W. Choi, I. Ryu, Y. Yao, M. T. McDowell, S. W. Lee, A. Jackson, Y. Yang, L. Hu, Y. Cui, *Nat. Nanotechnol.* **2012**, *7*, 310.

[5] N. Liu, Z. Lu, J. Zhao, M. T. McDowell, H.-W. Lee, W. Zhao, Y. Cui, *Nat. Nanotechnol.* **2014**, *9*, 187.

[6] X. W. Lou, Y. Wang, C. Yuan, J. Y. Lee, L. A. Archer, *Adv. Mater.* **2006**, *18*, 2325.

[7] J. S. Chen, X. W. D. Lou, *Small* **2013**, *9*, 1877.

[8] C. K. Chan, X. F. Zhang, Y. Cui, *Nano Lett.* **2008**, *8*, 307.

[9] J. F. M. Oudenhoven, L. Baggetto, P. H. L. Notten, *Adv. Energy Mater.* **2011**, *1*, 10.

[10] S.-H. Yu, S. H. Lee, D. J. Lee, Y.-E. Sung, T. Hyeon, *Small* **2016**, *12*, 2146.

[11] M. Naguib, J. Come, B. Dyatkin, V. Presser, P.-L. Taberna, P. Simon, M. W. Barsoum,

Y. Gogotsi, *Electrochem. commun.* **2012**, *16*, 61.

[12] J. Zhao, Y. Zhang, Y. Wang, H. Li, Y. Peng, *J. Energy Chem.* **2018**, *27*, 1536.

[13] X. Wang, Z. Na, D. Yin, C. Wang, Y. Wu, G. Huang, L. Wang, *ACS Nano* **2018**, *12*, 12238.

[14] P. Zhu, Z. Zhang, S. Hao, B. Zhang, P. Zhao, J. Yu, J. Cai, Y. Huang, Z. Yang, *Carbon N. Y.* **2018**, *139*, 477.

[15] Y. Lu, J.-P. P. Tu, Q.-Q. Q. Xiong, J.-Y. Y. Xiang, Y.-J. J. Mai, J. Zhang, Y.-Q. Q. Qiao, X.-L. L. Wang, C.-D. D. Gu, S. X. Mao, *Adv. Funct. Mater.* **2012**, *22*, 3927.

[16] S. Chen, F. Wu, L. Shen, Y. Huang, S. K. Sinha, V. Srot, P. A. van Aken, J. Maier, Y. Yu, *ACS Nano* **2018**, *12*, 7018.

[17] D. Sun, X. Zhu, B. Luo, Y. Zhang, Y. Tang, H. Wang, L. Wang, *Adv. Energy Mater.* **2018**, *8*, 1801197.

[18] X. Feng, M. Tang, S. O'Neill, Y.-Y. Hu, *J. Mater. Chem. A* **2018**, *6*, 22240.

[19] M. Kong, H. Song, J. Zhou, *Adv. Energy Mater.* **2018**, *8*, 1801489.

[20] S. Carenco, D. Portehault, C. Boissière, N. Mézailles, C. Sanchez, *Chem. Rev.* **2013**, *113*, 7981.

[21] P. Mei, J. Kim, N. A. Kumar, M. Pramanik, N. Kobayashi, Y. Sugahara, Y. Yamauchi, *Joule* **2018**, *2*, 2289.

[22] K. N. Dinh, Q. Liang, C.-F. Du, J. Zhao, A. I. Y. Tok, H. Mao, Q. Yan, *Nano Today* **2019**, *25*, 99.

[23] S. H. Yang, W. J. Chung, S. McFarland, S. W. Lee, *Chem. Rec.* **2013**, *13*, 43.

[24] D. Oh, J. Qi, Y.-C. Lu, Y. Zhang, Y. Shao-Horn, A. M. Belcher, *Nat. Commun.* **2013**, *4*, 2756.

[25] K. T. Nam, D.-W. Kim, P. J. Yoo, C.-Y. Chiang, N. Meethong, P. T. Hammond, Y.-M. Chiang, A. M. Belcher, *Science* **2006**, *312*, 885.

[26] Y. J. Lee, H. Yi, W.-J. Kim, K. Kang, D. S. Yun, M. S. Strano, G. Ceder, A. M.

Belcher, *Science (80-.).* **2009**, *324*, 1051.

[27] M. Moradi, Z. Li, J. Qi, W. Xing, K. Xiang, Y. M. Chiang, A. M. Belcher, *Nano Lett.* **2015**, *15*, 2917.

[28] G. Zhang, S. Wei, A. M. Belcher, *ACS Appl. Nano Mater.* **2018**, 5631.

[29] J. F. Ohmura, F. J. Burpo, C. J. Lescott, A. Ransil, Y. Yoon, W. C. Records, A. M. Belcher, *Nanoscale* **2019**, *11*, 1091.

[30] W. C. Records, Y. Yoon, J. F. Ohmura, N. Chanut, A. M. Belcher, *Nano Energy* **2019**, *58*, 167.

[31] M. Schlesinger, in *Mod. Electroplat.*, John Wiley & Sons, Inc., Hoboken, NJ, USA, **2011**, pp. 447–458.

[32] H. Okamoto, *J. Phase Equilibria Diffus.* **2014**, *35*, 105.

[33] Q. Guan, W. Li, *J. Catal.* **2010**, *271*, 413.

[34] X. Wang, H.-M. Kim, Y. Xiao, Y.-K. Sun, *J. Mater. Chem. A* **2016**, *4*, 14915.

[35] Y. Pan, Y. Y. Liu, J. Zhao, K. Yang, J. Liang, D. D. Liu, W. Hu, D. D. Liu, Y. Y. Liu, C. Liu, *J. Mater. Chem. A* **2015**, *3*, 1656.

[36] R. W. Hart, H. S. White, B. Dunn, D. R. Rolison, *Electrochem. commun.* **2003**, *5*, 120.

[37] D. Deng, *Energy Sci. Eng.* **2015**, *3*, 385.

[38] J. Ma, S. Ni, X. Lv, X. Yang, L. Zhang, *Mater. Lett.* **2014**, *133*, 94.

[39] G. Li, H. Yang, F. Li, J. Du, W. Shi, P. Cheng, *J. Mater. Chem. A* **2016**, *4*, 9593.

[40] W. Lai, C. K. Erdonmez, T. F. Marinis, C. K. Bjune, N. J. Dudney, F. Xu, R. Wartena, Y.-M. Chiang, *Adv. Mater.* **2010**, *22*, E139.

[41] Y. Peng, Z. Le, M. Wen, D. Zhang, Z. Chen, H. Bin Wu, H. Li, Y. Lu, *Nano Energy* **2017**, *35*, 44.

[42] R. Inada, R. Kumasaka, S. Inabe, T. Tojo, Y. Sakurai, *J. Electrochem. Soc.* **2019**, *166*, A5157.

[43] Z. Deng, Z. Zhang, Y. Lai, J. Liu, J. Li, Y. Liu, *J. Electrochem. Soc.* **2013**, *160*, A553.

[44] D. Aurbach, B. Markovsky, A. Rodkin, E. Levi, Y. . Cohen, H.-J. Kim, M. Schmidt, *Electrochim. Acta* **2002**, *47*, 4291.

[45] M. D. Levi, G. Salitra, B. Markovsky, H. Teller, D. Aurbach, U. Heider, L. Heider, *J. Electrochem. Soc.* **1999**, *146*, 1279.

[46] Y. Zhu, J. G. Connell, S. Tepavcevic, P. Zapol, R. Garcia-Mendez, N. J. Taylor, J. Sakamoto, B. J. Ingram, L. A. Curtiss, J. W. Freeland, D. D. Fong, N. M. Markovic, *Adv. Energy Mater.* **2019**, 1803440.

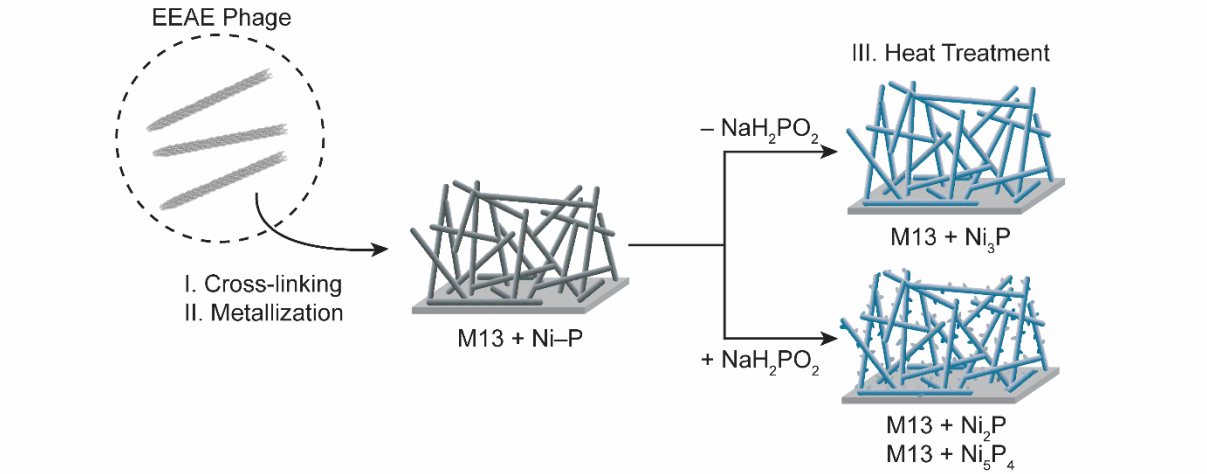

Figure 1. Schematic of the synthesis steps for virus-templated nickel phosphide nanofoams.

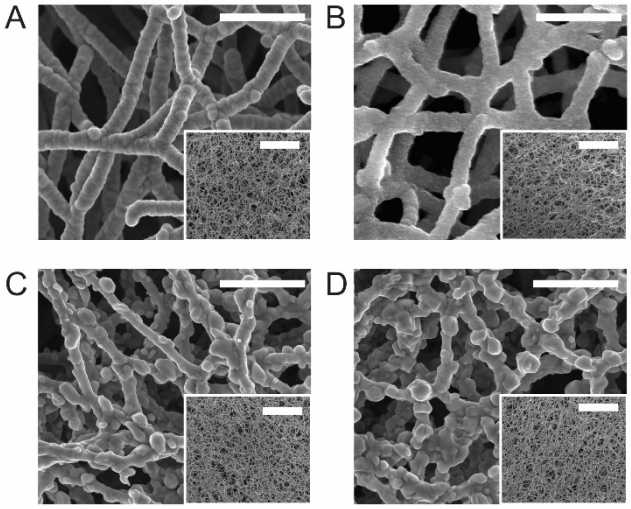

Figure 2. SEM characterization of pristine virus-templated nickel phosphide nanofoams showing an interconnected, contiguous nanowire morphology. Low- and high-magnification SEM images of (a) Ni–P, (b) Ni_3P, (c) Ni_2P, and (d) Ni_5P_4 nanofoams. Scale bars are 1 μm (insets: 10 μm).

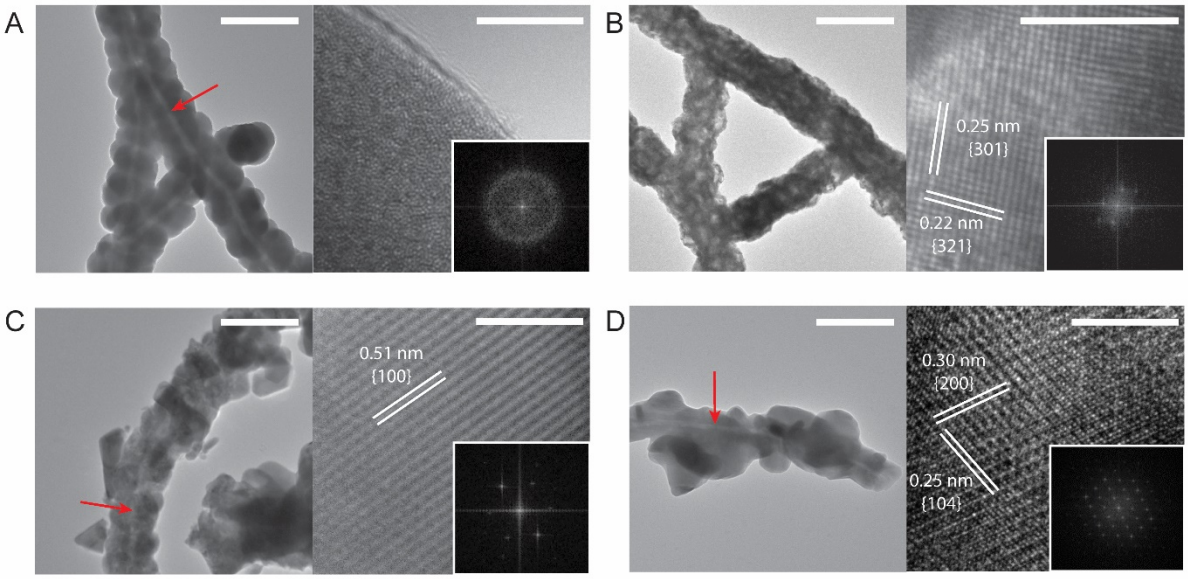

Figure 3. TEM characterization of pristine virus-templated metal phosphide nanofoams. TEM images (left), HRTEM images (right), and FFT patterns (right, inset) of (a) Ni–P, (b) Ni_3P, (c) Ni_2P, and (d) Ni_5P_4 nanofoams. Reported lattice spacings match PDF card numbers 00-004-0850, 04-015-7502, 04-003-1863, and 04-014-7901, respectively. Scale bars are 200 nm (left) and 5 nm (right). Red arrows indicate the virus-containing core of the nanofoam struts.

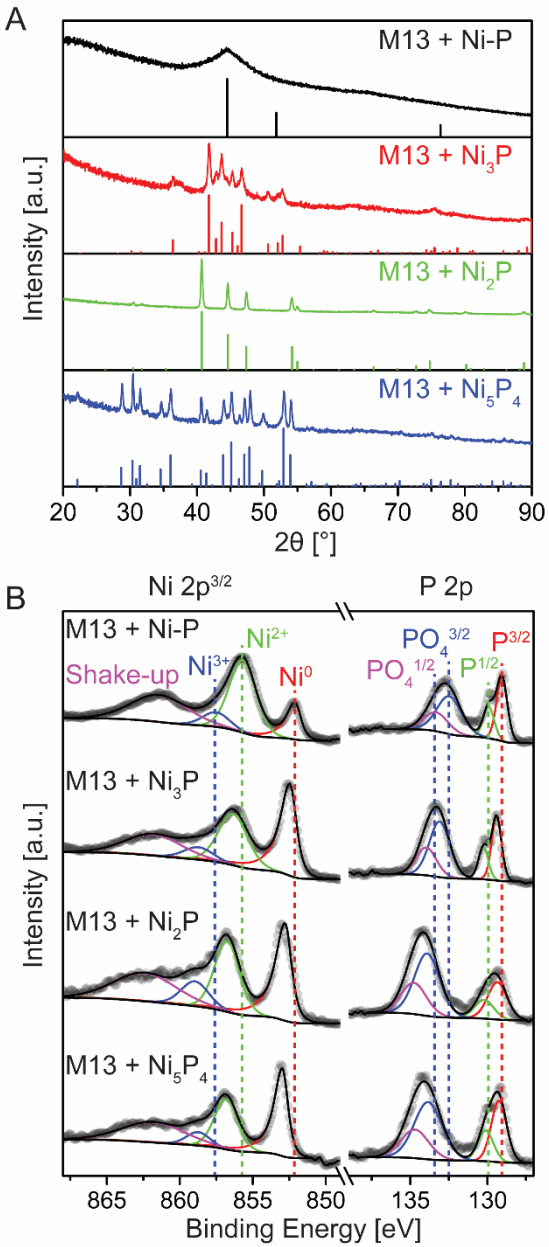

Figure 4. Crystallographic and surface characterization of virus-templated nickel phosphide nanofoams. (a) XRD scans for Ni–P, Ni_3P, Ni_2P, and Ni_5P_4 phases, matching PDF card numbers 00-004-0850, 04-015-7502, 04-003-1863, and 04-014-7901, respectively. (b) XPS scans of pristine, virus-templated Ni–P, Ni_3P, Ni_2P, and Ni_5P_4 nanofoams.

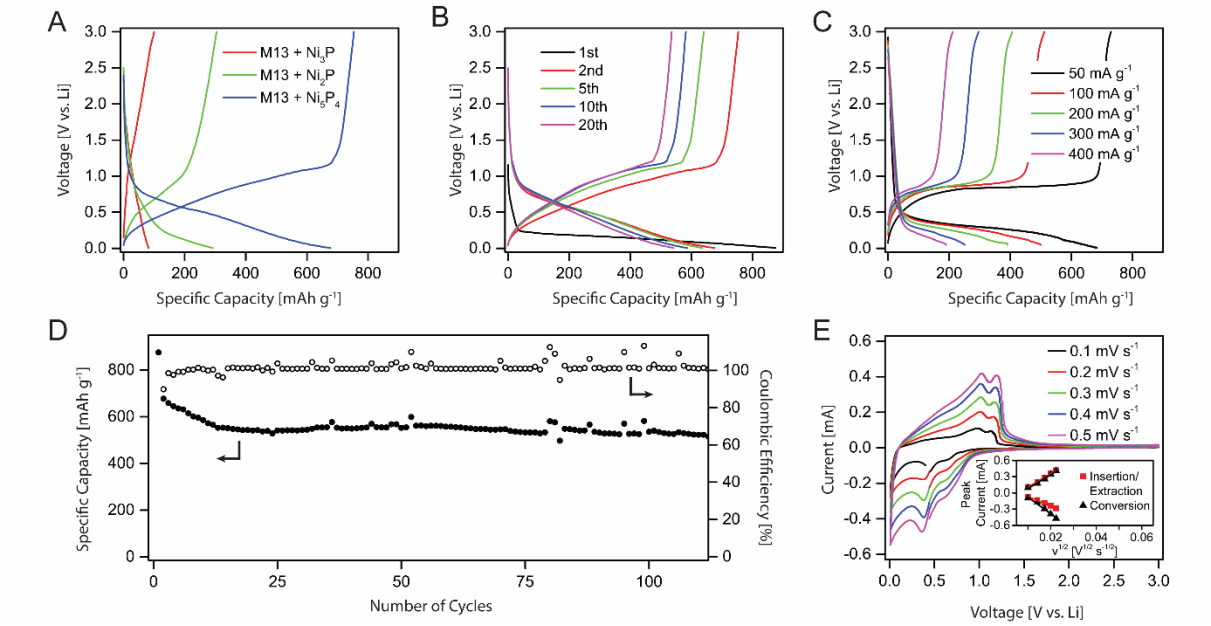

Figure 5. Electrochemical performance of virus-templated Ni_5P_4 nanofoam anodes. Voltage profiles of Ni_5P_4 anodes (a) against different nickel phosphide phases, (b) after cycling, and (c) at increasing cycling rates. (d) Overall cycling performance at a 50 mA g^{-1} rate with capacity stabilizing around 540 mAh g^{-1}. (e) Cyclic voltammograms at increasing scan rates (inset: fitting of oxidation and reduction peaks using the Randles–Sevik Equation).

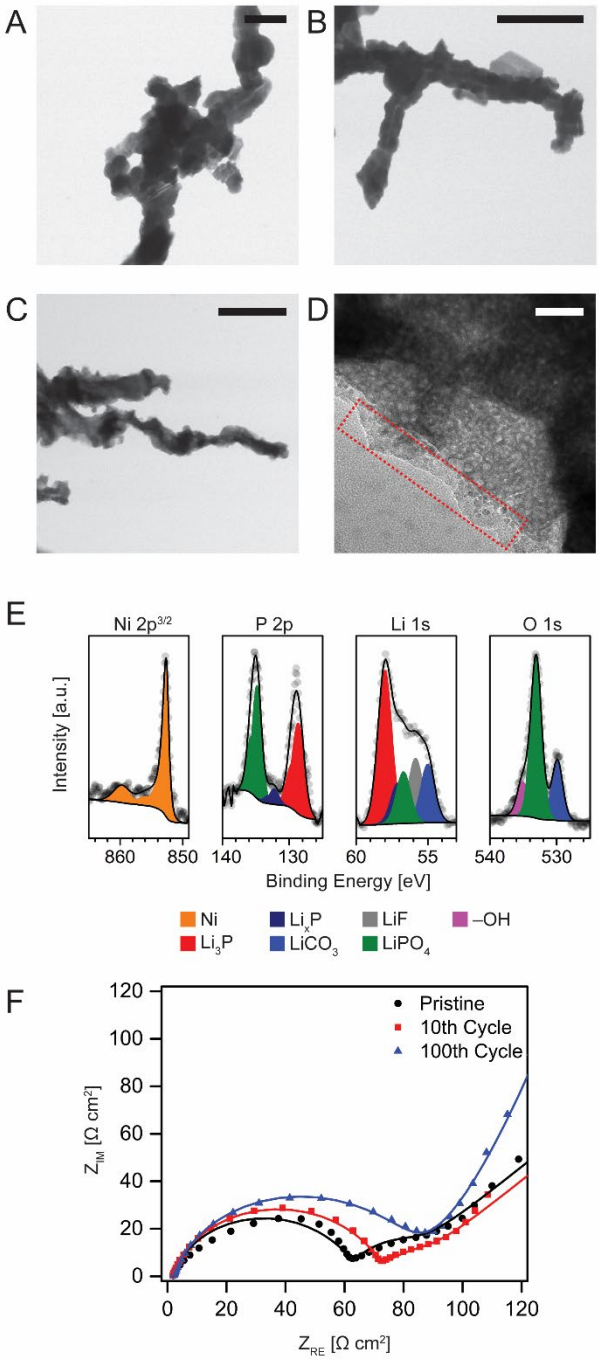

Figure 6. Post-cycling characterization and analysis of virus-templated Ni_5P_4 electrodes. Bright-field STEM images of virus-templated Ni_5P_4 nanofoam anodes after (a) first discharge, (b) first charge, and (c) 100th discharge. (d) TEM image showing the formation of an SEI layer (dotted red box) and surface roughening of a virus-templated nanowire discharged after 100 cycles, and corresponding (e) e*x situ* XPS analysis. (f) Electrochemical impedance spectra of pristine and cycled electrodes, as well as equivalent circuit fits. Scale bars for (a)–(d) are 500 nm, 1 µm, 1 µm, and 50 nm, respectively.

Table 1. Morphological and compositional characterization of virus-templated nickel phosphide nanofoams

Material	Thickness [µm][a)]	Ni [at%][b)]	P [at%][b)]
M13 + Ni–P	18.4 ± 3.0	78.4 ± 0.1	21.6 ± 0.1
M13 + Ni_3P	9.1 ± 1.3	78.0 ± 0.3	22.0 ± 0.3
M13 + Ni_2P	6.2 ± 1.9	63.7 ± 0.6	36.3 ± 0.6
M13 + NI_5P_4	6.6 ± 0.6	57.4 ± 0.1	42.6 ± 0.1

[a)]Standard error is reported as the measurement error on a single sample; [b)]Standard deviations are reported as the standard deviation of three samples, measured with ICP–AES.

Transition metal phosphides (TMP) are promising lithium-ion electrode materials. However, TMP syntheses remain underdeveloped regarding simultaneous control over phase composition and nanostructure. Here, M13 bacteriophage is employed to develop 3D nickel phosphide nanofoams with controllable phase composition and structural elements. Virus-templated nanofoams are integrated as additive-free, thin-film, lithium-ion microbattery electrodes. Virus-templating could enable further TMP development in energy storage.

Keyword: biotemplated metal phosphide

W. C. Records, S. Wei, A. M. Belcher*

Virus-templated nickel phosphide nanofoams as additive-free, thin-film Li-ion microbattery anodes